

Orientational Order of Colloidal Disk-Shaped Particles under Shear-Flow Conditions: a Rheological–Small-Angle X-ray Scattering Study

Isabelle Bihannic,^{*,†} Christophe Baravian,^{*,‡} Jérôme F. L. Duval,[†] Erwan Paineau,[†] Florian Meneau,[§] Pierre Levitz,^{||} Johann Patrick de Silva,[⊥] Patrick Davidson,[⊥] and Laurent J. Michot[†]

Laboratoire Environnement et Minéralurgie, Nancy University, CNRS, UMR 7569, BP40 54501 Vandœuvre Lès Nancy Cedex, France, Laboratoire d'Energétique et de Mécanique Théorique et Appliquée, Nancy University, CNRS, UMR 7563, 2 Avenue de la Forêt de Haye, BP160, 54504 Vandœuvre Lès Nancy Cedex, France, Soleil, L'Orme des Merisiers Saint-Aubin, BP 48, 91192 Gif-sur-Yvette Cedex, France, Laboratoire de Physique de la Matière Condensée CNRS, Ecole Polytechnique, UMR 7643, 91128 Palaiseau Cedex, France, and Laboratoire de Physique des Solides CNRS, Université Paris-Sud, UMR 8502, Bât 510, 91405 Orsay Cedex, France

Received: June 21, 2010; Revised Manuscript Received: October 15, 2010

The structure of a colloidal dispersion consisting of anisometric natural clay particles (beidellite) was followed under shear-flow conditions by small-angle X-ray scattering (SAXS) measurements in a Couette-type cell. It is shown that in this shear-thinning dispersion an orientational order develops with increasing shear rate. By use of two different geometrical configurations for SAXS measurements, corresponding to incident beam parallel and perpendicular to flow velocity gradient (radial and tangential configurations, respectively), it is observed that SAXS patterns are anisotropic in both geometries, meaning that particles tend to align along a preferred orientation with their normal in velocity gradient direction, and further they partly rotate around flow streamlines. Quantitative interpretation of these results is successfully achieved upon derivation of a probability distribution function accounting for biaxial particle orientation. From this distribution and following geometrical arguments, the viscosity of the suspension was calculated for each shear rate and found to correctly compare with rheological measurements, thereby appropriately relating the anisotropy of the SAXS patterns to macroscopic flow behavior of the suspension.

1. Introduction

The rheological behavior of colloidal suspensions evolves from Newtonian to visco-plastic^{1,2} with increasing particle volume fraction. The transition between these two regimes and the flow properties of the suspensions are determined by various parameters including interparticle forces, particle concentration, and particle size and shape. Compared to spherical colloids, anisometric particles exhibit non-Newtonian flow behavior at lower concentrations, due to their complex translational and rotational motions along the flow streamlines, which leads to shear-thinning properties. For example, suspensions of strongly anisometric platelike particles like natural clay minerals (typical aspect ratio between 25 and 1000) become non-Newtonian at particle volume fractions of about 0.2%^{3–10} and undergo a sol–gel transition at about 1%, with the appearance of yield stress and viscoelastic behavior. Recent extensive experimental work on suspensions of different swelling clays (nontronite,^{11–14} beidellite¹⁵) has further revealed the occurrence of a true isotropic/nematic phase transition at concentrations lower than the gelation thresholds. The particle interactions in these systems are mostly electrostatic repulsions^{13,14} and the rheological

properties can be quantitatively interpreted by considering the effects of excluded volume interactions on hydrodynamic viscous dissipation. In this approach, an effective hydrodynamic volume encompassing the particles may be defined and assimilated either to a sphere at low volume fractions or to an ellipsoid at higher volume fractions when spherical volumes would overlap. By use of such geometrical arguments, the evolution with clay concentration of both the interparticle distance and the infinite-shear viscosity can be adequately described.

Still, reaching a better understanding of shear-thinning in suspensions of platelike particles requires quantitatively investigating particle orientation under shear flow. Such an investigation can be numerically performed by use of simulation methods to compute platelet orbits under shear, with multiple hydrodynamic interactions taken into account.¹⁶ In the study reported here, we instead use an experimental method that consists of following by small-angle X-ray scattering (SAXS) the organization of suspensions sheared in situ in a Couette-type cell. Indeed, as already shown by various authors,^{7,17–19} such measurements provide direct insight into the relationship between microstructure, orientational order, and rheology.

With this in mind, we examined the flow behavior of a shear-thinning beidellite clay suspension at a concentration just below that of the isotropic/nematic phase transition (particle volume fraction = 0.4%). The ionic strength of the dispersion analyzed here is 10^{−5} mol/L, which corresponds to a purely repulsive system.^{10,13} In this paper, we present a model that relates the anisotropy of the SAXS patterns to the orientational distribution

* Corresponding authors: e-mail isabelle.bihannic@ensg.inpl-nancy.fr (I.B.) or christophe.baravian@ensem.inpl-nancy.fr (C.B.).

[†] Laboratoire Environnement et Minéralurgie, Nancy University.

[‡] Laboratoire d'Energétique et de Mécanique Théorique et Appliquée, Nancy University.

[§] Soleil, L'Orme des Merisiers Saint-Aubin.

^{||} Ecole Polytechnique.

[⊥] Université Paris-Sud.

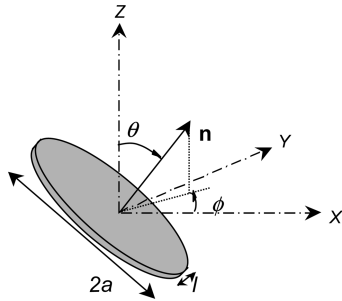


Figure 1

function of the particles in the shear flow. Subsequently, it is shown that, by use of this model, the suspension viscosity may be estimated in good agreement with the experimental rheological data. The paper is further organized as follows. In section 2.1, we give the expressions used to describe the particle orientational distribution functions. Then we calculate the intensity scattered by a collection of particles whose orientations follow these previously determined functions in section 2.2. These calculations are further discussed in order to relate SAXS pattern anisotropy and particle orientation (section 2.3). The details of the experimental setup used for measuring SAXS patterns under shear-flow conditions are then given. The corresponding measurements are first qualitatively discussed (section 3) and then quantitatively interpreted (section 4) on the basis of the model outlined in section 2.2.

2. Theory

In the field of liquid crystals, the nematic phase is commonly characterized by an orientational distribution function $f(\theta)$, which describes the distribution of orientations of the particles about a preferred direction, that is, the director of the nematic phase. Even if different forms of the orientational distribution function exist (for example, Maier–Saupe distribution^{20–22} or Onsager function²³), they all have in common dependence on only one variable, the angle θ between the particle axis and the nematic director. In this case, the problem is different and consists of determining the orientation of the particles under shear flow. The particle orientation is here defined by the two Euler angles θ and ϕ and the probability density function (PDF) relative to these angles. The object of this section is to derive a new expression of the PDF as a function of both Euler angles.

We consider a disklike particle of diameter $2a$ and thickness l as depicted in Figure 1. The outward normal unit vector \mathbf{n} associated with the particle is positioned in the XYZ coordinate system according to the polar and azimuthal angles, labeled θ ($\in [0, \pi]$) and ϕ ($\in [0, 2\pi]$), that are defined with respect to the Z and X axes, respectively (Figure 1).

2.1. Derivation of the Orientational Distribution Functions. The angles θ and ϕ , defined in Figure 1, may be considered as two random variables. The probability of finding a particle in a given orientation is then provided by the probability density functions (PDF) associated with the angles θ and ϕ , called $g_1(\theta)$ and $g_2(\phi)$, respectively.

In the simple situation where particles are randomly oriented due to free particle rotation, all orientations are equiprobable. As a result, the points (θ, ϕ) defining the orientations of the particle normals are uniformly distributed over a sphere (i.e., in 4π steradians). The probability of finding a particle normal pointing within the solid angle element $d\Omega$ is thus $(1/4\pi) \sin(\theta) d\theta d\phi$. Then, we have

$$g_1(\theta) = \frac{1}{2} \sin(\theta) \quad \text{and} \quad G_1(\theta) = \frac{1}{2} \int_0^\theta \sin(\theta) d\theta$$

and

$$g_2(\phi) = \frac{1}{2\pi} \quad \text{and} \quad G_2(\phi) = \frac{1}{2\pi} \int_0^\phi d\phi$$

where the functions $G_1(\theta)$ and $G_2(\phi)$ are the so-called cumulative distribution functions (CDF). Under shear, particles are no longer free to rotate, but instead an *asymmetrical preferred orientation* is observed, as will be illustrated in the Experimental Section. (Note that the simple shear-flow geometry, as achieved in a Couette shear cell, is intrinsically biaxial because the velocity, velocity gradient, and neutral directions are all different.) Under such conditions, the points (θ, ϕ) used to locate the particle normals are no longer uniformly distributed over a sphere, but instead their probability density functions must be altered to reflect the asymmetrical preferred orientation. This can be done by considering, instead of a sphere, a biaxial ellipsoid whose parametric equations in the XYZ coordinate system are given by

$$X = \cos(\phi) \sin(\theta)$$

$$Y = m_y \sin(\phi) \sin(\theta)$$

$$Z = m_z \cos(\theta)$$

where m_y and m_z are the ellipsoid semiaxes. The ellipsoid geometry is adopted because it is the most intuitive object built from a sphere and displaying a biaxial shape.

In order to derive the probability distribution functions for θ and ϕ in this geometry, the simplest way is to perform a change of variables so as to retrieve the formulation given above for the PDF in spherical geometry. Calling these new variables X' , Y' , Z' , θ' , and ϕ' , we obtain

$$X' = \frac{\cos(\phi) \sin(\theta)}{\{\sin^2(\theta)[\cos^2(\phi) + m_y^2 \sin^2(\phi)] + m_z^2 \cos^2(\theta)\}^{1/2}} = \cos(\phi') \sin(\theta')$$

$$Y' = \frac{m_y \sin(\phi) \sin(\theta)}{\{\sin^2(\theta)[\cos^2(\phi) + m_y^2 \sin^2(\phi)] + m_z^2 \cos^2(\theta)\}^{1/2}} = \sin(\phi') \sin(\theta')$$

$$Z' = \frac{m_z \cos(\theta)}{\{\sin^2(\theta)[\cos^2(\phi) + m_y^2 \sin^2(\phi)] + m_z^2 \cos^2(\theta)\}^{1/2}} = \cos(\theta')$$

and the angles θ' and ϕ' are related to θ and ϕ via

$$\theta' = \arccos(Z') = \arccos\left(\frac{m_z \cos(\theta)}{\{\sin^2(\theta)[\cos^2(\phi) + m_y^2 \sin^2(\phi)] + m_z^2 \cos^2(\theta)\}^{1/2}}\right) \quad (1)$$

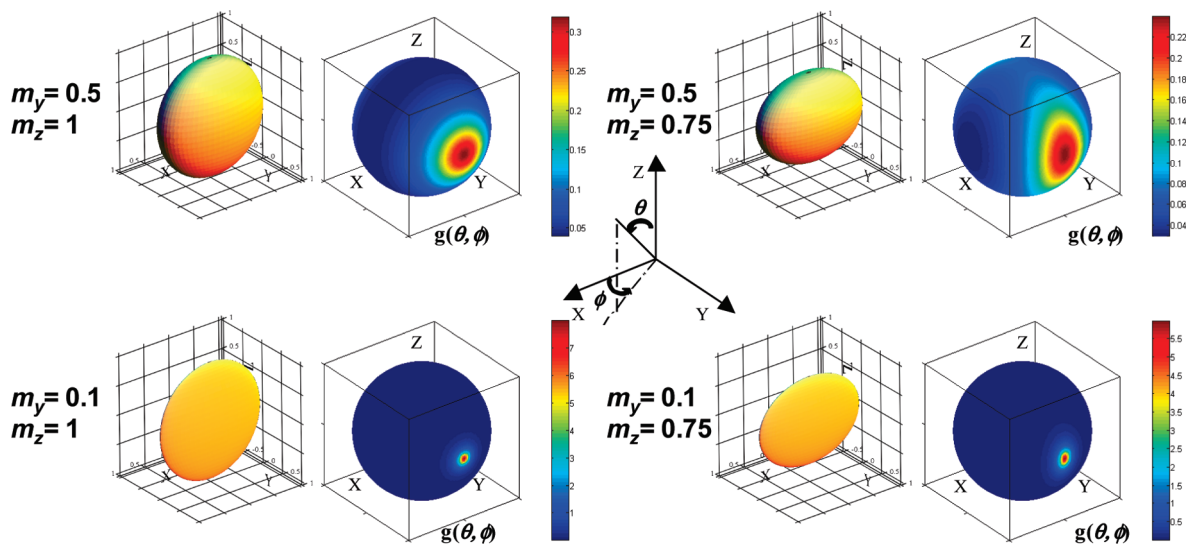


Figure 2. Plots of the ellipsoid and the PDF $g(\theta, \phi)$ for different values of m_y and m_z .

and

$$\phi' = \arctan\left(\frac{Y'}{X'}\right) = \arctan[m_y \tan(\phi)] \quad (2)$$

Assuming a uniform distribution of points defined by (θ', ϕ') over a sphere, it follows that the cumulative density functions for θ' and ϕ' are yielded by $G_1'(\theta') = (1/2) \int_0^{\theta'} \sin(\theta') d\theta'$ and $G_2'(\phi') = (1/2\pi) \int_0^{\phi'} d\phi'$, which can be rewritten in the form $G_1'(\theta') = \int_0^{\theta'} g_1(\theta) d\theta$ and $G_2'(\phi') = \int_0^{\phi'} g_2(\phi) d\phi$, respectively. After some developments, the angular functions g_1 and g_2 are provided by the following expressions:

$$g_1(\theta) = \frac{m_z \sin(\theta) [\cos^2(\phi) + m_y^2 \sin^2(\phi)]}{2 \{\sin^2(\theta) [\cos^2(\phi) + m_y^2 \sin^2(\phi)] + m_z^2 \cos^2(\theta)\}^{3/2}} \quad (3)$$

and

$$g_2(\phi) = \frac{1}{2\pi} \frac{m_y}{\cos^2(\phi) + m_y^2 \sin^2(\phi)} \quad (4)$$

where we used the relationships

$$\sin(\theta') d\theta' = \frac{\sin(\theta) [\cos^2(\phi) + m_y^2 \sin^2(\phi)]}{m_z \{\sin^2(\theta) [\cos^2(\phi) + m_y^2 \sin^2(\phi)] + m_z^2 \cos^2(\theta)\}^{3/2}} d\theta$$

and

$$d\phi' = \frac{m_y}{\cos^2(\phi) + m_y^2 \sin^2(\phi)} d\phi$$

as obtained by differentiating eqs 1 and 2, respectively. According to eqs 3 and 4, the probability that a disk will have its normal in the solid angle $d\Omega = \sin(\theta) d\theta d\phi$ is finally given

by

$$g(\theta, \phi) = \frac{g_1(\theta)g_2(\phi)}{\sin(\theta)} = \frac{m_y m_z}{4\pi \{\sin^2(\theta) [\cos^2(\phi) + m_y^2 \sin^2(\phi)] + m_z^2 \cos^2(\theta)\}^{3/2}} \quad (5)$$

which satisfies the normalization condition expressed by

$$\frac{1}{4\pi} \int_0^{2\pi} d\phi \int_0^\pi g(\theta, \phi) \sin(\theta) d\theta = 1$$

For the sake of illustration, typical dependences of the density distribution function on angles (θ, ϕ) are depicted in Figure 2 for different values of m_y and m_z . For each set (m_y, m_z) chosen, both the ellipsoid and the PDF $g(\theta, \phi)$ are given. The function $g(\theta, \phi)$ is represented over a sphere, at the surface of which a given point indicates its magnitude according to the color scales shown in Figure 2. We comment below on the typical features of $g(\theta, \phi)$ as a function of (m_y, m_z) .

2.1.1. $m_z = 1, m_y < 1$. We first examine calculation results for $m_z = 1$ with two different m_y values: $m_y = 0.5$ and $m_y = 0.1$ (Figure 2, left-hand side). As soon as m_y is strictly lower than 1, the ellipsoid flattens in the (XZ) plane. Meanwhile, the PDF presents a maximum value for $\theta = \pi/2$ and $\phi = \pi/2$, indicating that the particle normals orient preferentially in the y -axis direction. Upon decrease of m_y , the preferred orientation still follows the y -axis ($\theta = \pi/2$ and $\phi = \pi/2$), and the maximum of the PDF becomes sharper.

2.1.2. $m_z < 1, m_y < 1$. Illustrations are also shown for $m_z = 0.75$ (Figure 2, right-hand side), with the same m_y values as adopted in the previous case ($m_y = 0.5$ and 0.1). For m_z values lower than 1, the probability density function becomes asymmetric around the preferred direction: the spot that represents the most probable particle orientation displays a vertical anisotropy. This means that the particles are still preferentially aligned in the (XZ) plane but in addition they present a slight rotation movement around the X axis.

On the basis of the above-derived expression for the PDF, it is possible to calculate the probability that the 2D particle crosses

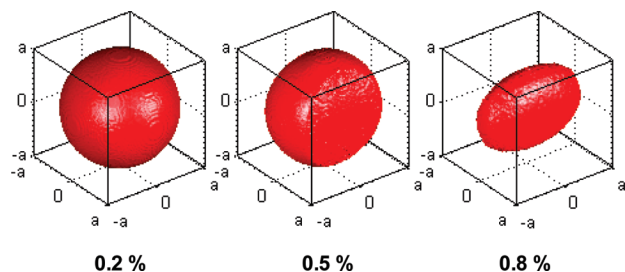


Figure 3. Statistical volume calculated for $m_z = 0.75$ and $m_y = 0.5$. All the points within this volume correspond to (X, Y, Z) coordinates that the disk crosses with a probability higher than the value indicated below the diagram (0.2%, 0.5%, and 0.8%).

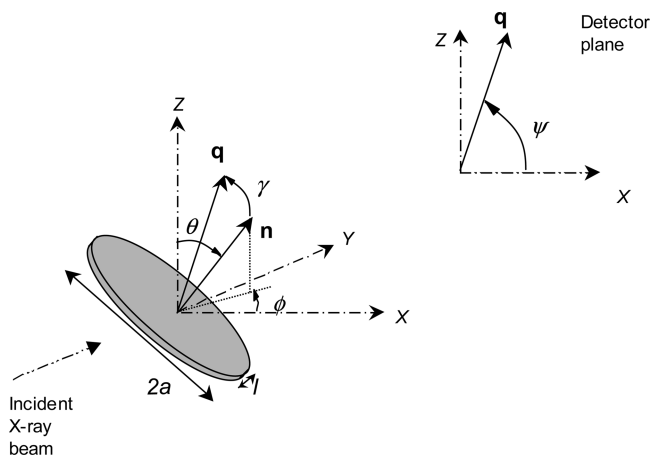


Figure 4. Experimental geometry.

a given position (X, Y, Z) . This is achieved by meshing a spatial region centered around the particle and subsequently summing the probability distribution function over the angular variables θ and ϕ for each (X, Y, Z) point. Accordingly, the origin of space that corresponds to the disk center has a probability of 1. This calculation was carried out for the set of parameters ($m_z = 0.75$, $m_y = 0.5$) and corresponding results are displayed in Figure 3, where isosurfaces of probability 0.2%, 0.5%, and 0.8% are displayed. Inspection of Figure 3 shows that the statistical volume within the isosurface adopts spherical geometry at very low values of the considered probability, essentially because there are no rejected orientations. Conversely, when this isosurface value is increased, the probability weight associated with the preferred angular orientations of the particles becomes larger, thereby flattening the particle statistical volume.

2.2. Intensity Scattered by Oriented Disk-Shaped Particles. This section deals with calculation of the intensity scattered by a set of disks whose orientations follow the distributions derived in the previous section. We use the following conventions for the beam direction and detector location with respect to the particle positioned in the XYZ system of coordinates previously defined: the vertical axis of the laboratory is the Z axis, the incident X-ray beam is parallel to the Y direction, and the detector stands in the (XZ) plane, as specified in Figure 4. This convention is similar to the one used in publications on related systems.^{7,17,18,24}

The scattered intensity is expressed as a function of the scattering vector \mathbf{q} , defined as the difference between the wave vector of the scattered beam and the wave vector of the incident beam ($\mathbf{q} = \mathbf{k} - \mathbf{k}_0$ and $q = 4\pi \sin \theta / \lambda$, where 2θ is the scattering angle and λ is the wavelength). Two additional angles, γ and ψ , are required to define the orientation of \mathbf{q} with respect to the particle normal \mathbf{n} and the X -axis of the detector, respectively.

Because the scattering angles are quite small, one can safely consider that \mathbf{q} lies in the (ZX) plane. Following geometrical arguments, we easily obtain

$$\cos \gamma = \cos \theta \sin \psi + \sin \theta \cos \psi \cos \phi$$

For monodisperse noninteracting particles in dilute suspension, the scattered intensity is calculated from the form factor, whose expression as a function of the scattering vector \mathbf{q} for a disk of thickness l and radius a is provided by²⁵

$$F(\mathbf{q}) = F(q, \gamma) = K_1 \frac{\sin(ql \cos \gamma/2)}{(ql \cos \gamma/2)} \frac{2J_1(qa \sin \gamma)}{(qa \sin \gamma)} \quad (6)$$

where K_1 is a constant that includes particle volume and number of particles as well as the contrast in electron density between particles and solvent. J_1 is the first-order Bessel function of the first kind. The scattered intensity is then calculated by averaging the form factor, which leads to

$$I(\mathbf{q}) = K_2 \langle [F(\mathbf{q})]^2 \rangle \quad (7)$$

where K_2 is an experimental constant and the angular brackets denote an average over particle orientations. In order to take into account the orientation distribution, we amend eq 7 by including the orientation distribution function $g(\theta, \phi)$. Finally, the expression of the scattered intensity is²⁶

$$I(\mathbf{q}) = I(q, \psi) = K_2 \int_0^{2\pi} \int_0^\pi [F(q, \gamma)]^2 g(\theta, \phi) \sin(\theta) d\theta d\phi \quad (8)$$

2.3. Simulations of SAXS Patterns. On the basis of eq 8, the scattered intensity was calculated for individual disks of diameter $2a \approx 210$ nm and thickness $l \approx 0.65$ nm.

As will be detailed in the Experimental Section, two geometrical configurations were used to record the SAXS patterns. We first need to define these geometries to calculate the scattered intensity. The first geometry, which will be called “radial geometry”, corresponds to the situation where the velocity gradient is parallel to the incident beam direction. In that case the disk normal is aligned along the Y axis (i.e., the incident beam) and eq 8 is used straightforwardly. The second situation, referred to as “tangential geometry”, is that where the particles stand parallel to the beam direction. This means that the disk normal and the velocity gradient are now perpendicular to the beam direction. The streaming plane defined by the velocity and the velocity gradient is now rotated by an angle of $\pi/2$ with regard to the previous configuration. Equation 8 is used to calculate the SAXS patterns after a phase shift of $\pi/2$ is introduced for the ϕ angle. Given these definitions, the scattered intensity was calculated for different values of m_y and m_z , in both tangential and radial geometries.

Let us first comment on the simplest case where particles are randomly oriented, that is, $m_y = m_z = 1$. The general expression for randomly oriented disks is then retrieved,³⁰ and the calculated patterns are isotropic, as expected, in both tangential and radial geometries (not shown). According to the arguments given in section 2.1, a preferential orientation is obtained, provided that $m_y < 1$.

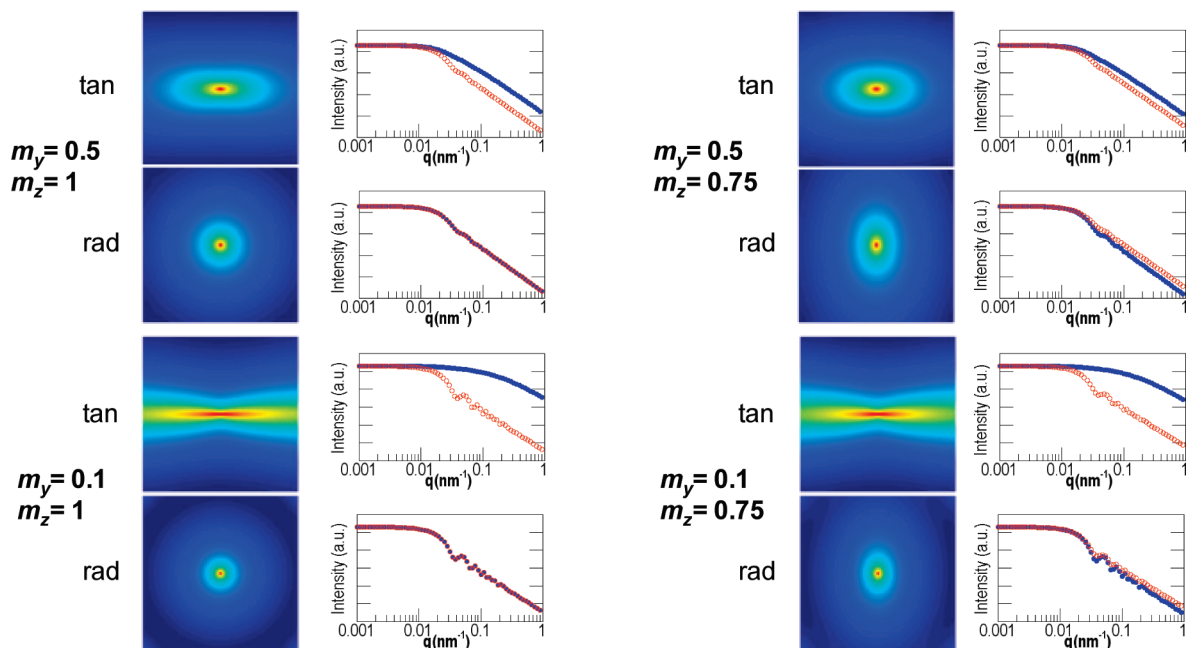


Figure 5. Simulation results for a set of different values of m_y and m_z ($m_y = 0.5$ and $m_z = 1$; $m_y = 0.1$ and $m_z = 1$; $m_y = 0.5$ and $m_z = 0.75$; $m_y = 0.1$ and $m_z = 0.75$): calculated SAXS 2D patterns, with the corresponding $\log(I)$ vs $\log(q)$ curves calculated either horizontally (blue solid circles) or vertically (red open circles).

Results collected in Figure 5 are calculated for the same values of m_y and m_z as used in Figure 2. Moreover, plots of scattered intensity versus scattering vector modulus are given in the horizontal and vertical directions of the patterns, that is, at $\psi = 0$ and $\pi/2$, respectively.

2.3.1. $m_z = 1$, $m_y < 1$. For $m_z = 1$ and $m_y < 1$, we showed in section 2.1 that particles orient with their normal along the Y (respectively X) direction in the radial (respectively tangential) geometry, with a uniform distribution around this preferred direction. As far as the 2D SAXS patterns are concerned (Figure 5, left-hand side), this results in a scattering anisotropy where the intensity decays more slowly along the horizontal direction than in the vertical one in the tangential geometry, whereas the patterns remain isotropic, in radial geometry, whatever the value of m_y .

In the tangential geometry, for a given scattering vector modulus q , intensities calculated along the horizontal direction are larger than those calculated in the vertical one, an effect that of course increases with increasing pattern anisotropy. This results from the mathematical formulation of the form factor: the first term involved in eq 6 is of the form $\sin(x)/x$ and is a function of the disk thickness, while the second term is of the form $J_1(y)/y$ and is a function of the disk radius. For oriented systems, the intensity along the horizontal direction is governed by the first term, whereas it is governed by the second one along the vertical direction.

The curves calculated along the horizontal direction in the radial geometry correspond to those obtained along the vertical direction in the tangential geometry.

2.3.2. $m_z < 1$, $m_y < 1$. In this case, the probability density functions are asymmetric around the preferred direction (Figure 2). This gives rise to some anisotropy of the 2D patterns calculated in radial geometry (Figure 5). Meanwhile, scattering patterns in tangential geometry are slightly less anisotropic as compared to those evaluated for similar values of m_y when $m_z = 1$.

3. Experimental Section

In order to test the previous model, small-angle X-ray scattering has been used to probe the structure of a suspension of disklike clay particles under shear-flow conditions. Experiments were performed with a Couette shear cell, and SAXS patterns were recorded at different shear rates so as to follow the rearrangement of the particles with shear.

3.1. Materials. The clay used in these experiments is a natural beidellite SBId-1 supplied from the Source Clays Minerals Repository of the Clay Mineral Society at Purdue University. Beidellite is a dioctahedral swelling clay mineral, whose average structural formula is¹⁵ $(\text{Si}_{7.26}\text{Al}_{0.74})(\text{Al}_{3.74}\text{Fe}_{0.2}\text{Mg}_{0.14})\text{O}_{20}(\text{OH})_4\text{Na}_{0.66}$. The charge of the individual particles originates from the substitution of silicon by aluminum in the tetrahedral layer. Before use, the clay was purified to remove accessory minerals and subsequently homoionized with sodium cations. The full procedure for purification and fractionation is described elsewhere.^{12,15} To minimize size polydispersity, the purified sodium-exchanged bulk suspension was centrifuged under different gravitational fields. Three size fractions were then obtained.²⁷ After fractionation, the dilute suspension was concentrated by osmotic stress, a procedure that consists of placing the suspension in dialysis membranes (Visking, 14 000 Da) that were then immersed for 1 month in a poly(ethylene glycol) (PEG) solution. The studied sample corresponds to the smallest size fraction with a mean diameter of 210 nm and a polydispersity of 38%.¹⁵ The value of the osmotic pressure was imposed by the PEG concentration (4 g/L in the present case, yielding an osmotic pressure of ≈ 500 Pa). The ionic strength of the electrolyte (NaCl) was fixed at 10^{-5} M/L. After osmotic stress, the solid concentration was determined by drying an aliquot of the sample. The concentration of the present sample is 11 g/L, corresponding to a volume fraction of 0.4%.

3.2. Experimental Methods: Small-Angle X-ray Scattering. Small angle scattering experiments (SAXS) were carried out under shear on beamline SWING at the Soleil synchrotron facility (Saclay, France). Measurements were performed at a wavelength of 0.11 nm, with a two-dimensional detector placed

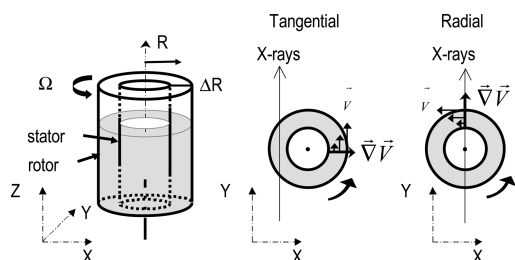


Figure 6. Schematic drawing of the Couette cell and configurations for SAXS measurements.

at a distance of 6 m from the sample. The resulting accessible q -range was from 0.02 to 0.8 nm⁻¹. SAXS data were acquired with the newly developed AVIEX 170170 charge-coupled device (CCD) detector, placed in a vacuum detection tunnel. The transmitted intensity was recorded simultaneously with SAXS data acquisition, with a diode inserted in the beamstopper, in order to perform accurate data normalization. The X-ray beam size was 300 μm × 100 μm.

A homemade Couette shear-cell apparatus was specially developed to combine rheological and *in situ* SAXS experiments.²⁷ It consists of a static inner cylinder (stator) (10 mm radius) and a rotating outer cylinder (rotor), both made of polycarbonate, thereby defining a gap width of 0.5 mm. The rotor speed is controlled by a motor, with a corresponding shear rate that may be varied from 1.25 to 5000 s⁻¹. Scattering patterns were recorded at different shear-rate values through three stages: starting with a static initial state at rest, followed by a stage of increasing shear rates up to 5000 s⁻¹, and a final stage of shear rates decreasing from 5000 to 1.25 s⁻¹. The whole procedure lasts 30 min. For each shear-rate value, measurements were performed both in radial geometry (with the X-ray beam passing through the cell center) and in tangential geometry (X-ray beam perpendicular to the velocity gradient) (Figure 6). Patterns were recorded with an exposure time of 800 ms, a few seconds after the shear rate was set at the desired value, in order to avoid transitional flow effects.

Scattering patterns recorded as a function of shear rate are displayed in Figure 7. The contribution of the Couette cell filled with water to the scattering was subtracted after appropriate correction from transmission. (The black cross on the patterns of Figure 7 is an artifact due to the boundaries between the

different parts of the CCD camera.) Starting from the situation where patterns are isotropic at rest, a clear dependence of the patterns on shear rate is observed in the tangential geometry. The SAXS diffuse halo extends more and more along the horizontal direction with increasing shear rate. This anisotropy gradually vanishes when the shear rate is decreased. Indeed, the last pattern recorded at 1.25 s⁻¹ is almost isotropic. This horizontal anisotropy reflects the alignment of the particles with their normals along the X direction, as defined in Figure 6. Moreover, upon inspection of the patterns measured in radial geometry, it is clear that the scattering extends further along the vertical direction, an effect that increases with increasing shear rate. This indicates that the orientation distribution is actually biaxial because it is not fully symmetrical around the direction of the velocity gradient. However, for a given shear rate, this anisotropy is less pronounced than that observed in the tangential geometry.

For both geometries (radial and tangential), integration of the scattering patterns in Figure 7, over an angular range of 30° in the horizontal ($\psi = 0$) and vertical ($\psi = \pi/2$) directions, gives the scattered intensity (expressed in arbitrary units) as a function of the scattering vector modulus q ($q = 4\pi \sin \theta/\lambda$, where 2θ is the scattering angle and λ is the wavelength) along the X and Z directions. These results are presented in Figure 8 for some selected shear rates. In all cases, the scattered intensity essentially follows a q^{-2} dependence as expected for two-dimensional scattering objects that show enough orientational disorder. Furthermore, a slight intensity modulation is observed at low q values, which is attributed to positional correlations between particles (i.e., a structure factor). This modulation is most visible on the intensity curve measured horizontally in tangential geometry (Figure 8B). Besides, the anisotropy of the scattering patterns induces a shift in intensity of the scattering curves.

In addition, viscosity measurements were carried out by use of a rheometer of cone plane geometry (AR2000 rheometer, TA Instruments, angle 0.3°, diameter 20 mm, truncation 14 μm).

4. Analysis of Experimental Scattering Patterns

In order to interpret the experimental scattering patterns in terms of orientational field, a complete set of 2D patterns was computed for different values of m_y and m_z on the basis of the

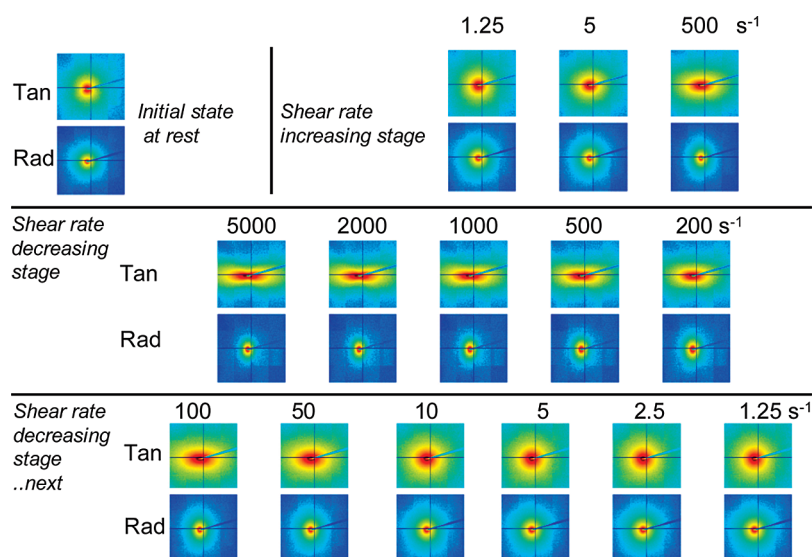


Figure 7. SAXS patterns recorded for different shear-rate values, in both tangential and radial configurations.

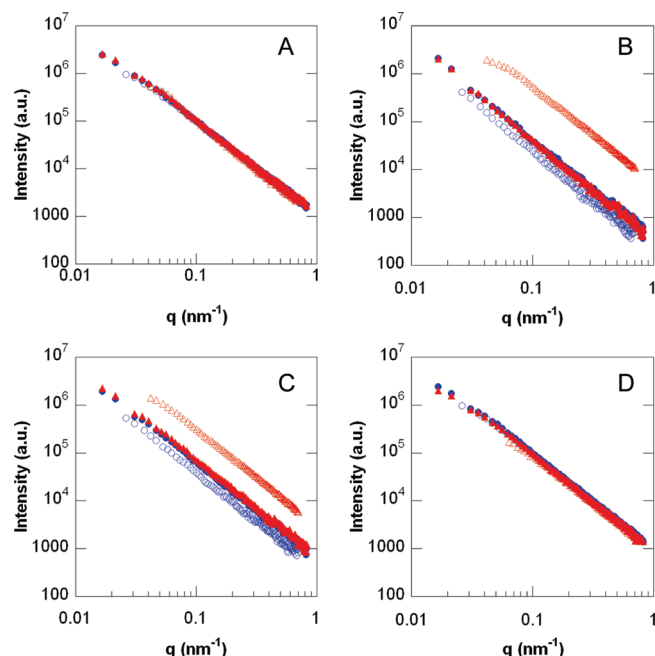


Figure 8. Evolution of intensity as a function of q (in log scales) for some specific shear rates: (A) static initial state, (B) 5000 s⁻¹, (C) 200 s⁻¹, and (D) 1.25 s⁻¹. The four curves correspond to different angular integration (horizontally and vertically) on patterns measured in both radial and tangential modes: (solid blue circles) radial vertical; (open blue circles) radial horizontal; (solid red triangles) tangential vertical; (open red triangles) tangential horizontal.

model presented in section 2. Calculations were carried out for the geometric features of the beidellite particles (radius 105 nm, thickness 0.65 nm¹⁵). By use of such a database and by comparison with experimental results, the values of m_y and m_z could be determined for each scattering pattern. The uniqueness of the set of parameters m_y and m_z for a given pattern could be

quantitatively addressed by careful examination of (i) the intensity dependence as a function of q for two values of ψ (0 and $\pi/2$) and (ii) the angular intensity scans as a function of ψ for a particular value of q (0.1 nm⁻¹). As discussed in section 2, the parameter m_y does not affect the anisotropy of the patterns in the radial geometry, so that the first step of the modeling consisted of determining m_z in this case. This procedure was then applied to the tangential geometry; the overall fitting procedure thus consisted of comparing six experimental curves with six theoretically calculated ones. Figure 9 illustrates such a comparison for two different shear-rate values.

In Figure 9A, the experimental intensity is compared to calculations for two different values for the particle radius: $a = 105$ nm, which corresponds to the mean radius of the beidellite size fraction of interest here,²⁷ and $a = 200$ nm. The agreement between experiment and calculation is better for the larger size at low q values: for $a = 105$ nm, the scattered intensity reaches the Guinier plateau for a q value of 0.01 nm⁻¹, which affects the overall shape of the intensity curves. For $a = 200$ nm, the plateau is observed for a smaller q value and there is better agreement between the slopes of the calculated curve and the experimental one over the whole q -range investigated. Rigorously speaking, calculations should have been performed by taking into account the whole size polydispersity (38%)¹⁵ of the clay fraction, and the scattered intensity would then be an average of all the intensities calculated for each radius of the distribution, weighted by the volume of each particle. As this process is very tedious and time-consuming, calculations were performed only with the mean radius of the distribution, that is, 105 nm.

It must also be pointed out that the model completely neglects the structure factor. This assumption can safely be made because the modulation best observed in Figure 8B is very weak.

The parameters (m_y , m_z) derived for each shear rate are summarized in Table 1. We estimate the errors in m_y and m_z to

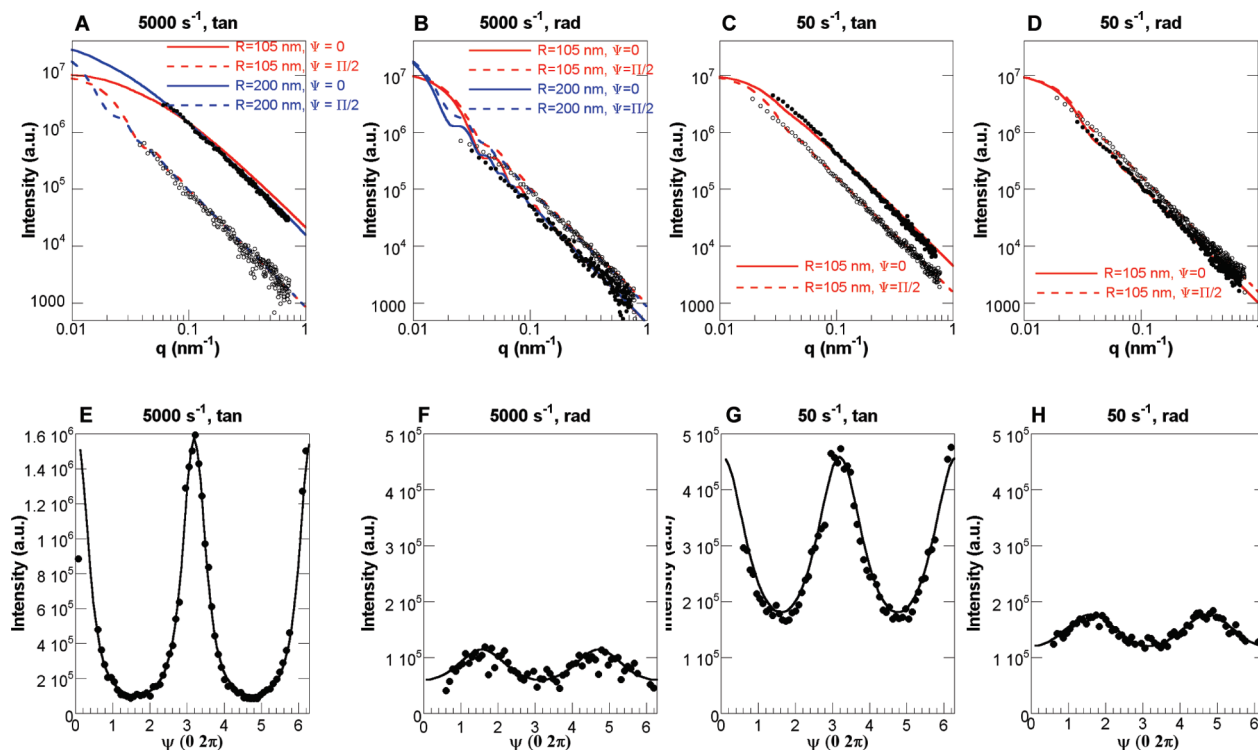


Figure 9. (A–D) Comparison of calculated and experimental intensities as a function of q for two values of Ψ : (●) $\Psi = 0$; (○) $\Psi = \pi/2$. (E–H) Angular intensity scan as a function of Ψ for a value of q of 0.1 nm⁻¹: (●) experiment; (—) calculation.

TABLE 1: Parameters Derived for Different Shear Rates

	shear rate (s ⁻¹)											
	5000	2000	1000	500	200	100	50	20	10	5	2.5	1.25
m_y	0.26	0.29	0.32	0.37	0.46	0.52	0.6	0.75	0.82	0.88	0.92	0.95
m_z	0.77	0.77	0.78	0.80	0.81	0.85	0.86	0.91	0.94	0.96	1	1

be about $\pm 10\%$ of the values indicated in Table 1. The determined values are used in the following section to relate the particle orientation under shear and the corresponding suspension viscosity.

5. Relationship between Shear-Induced Particle Orientation and Hydrodynamic Dissipation

The methodology developed in the present paper allows for retrieving the mean orientation of 2D particles subjected to shear flow. This is necessary to link microscopic organization with macroscopic properties such as shear-induced optical birefringence or viscous dissipation. In the latter case, it may be thought that modeling the suspension shear-thinning behavior would require hydrodynamic calculations, as first proposed by Jeffery²⁸ in a Fokker–Planck-type formalism.²⁹ In order to demonstrate the relevance of the methodology proposed here, we report preliminary calculations of the viscosity of the suspensions on the basis of a semiempirical effective approach, which underlines the relationship between particle orientation under shear and the corresponding viscosity.

As a starting point, the hydrodynamic drag dissipation of randomly oriented particles ($m_y = m_z = 1$) in a flow field is assimilated to that of the hydrodynamic spheres encompassing the particles. In the present case, when the average dimensions of the particles and their volume fractions (ϕ_{disk}) are taken into account, the effective volume fraction of such spheres (denoted ϕ_{sphere}) is equal to $0.86 [\phi_{\text{sphere}} = \phi_{\text{disk}}(4/3)(a/l)]$, where $a = 105$ nm and $l = 0.65$ nm are the radius and thickness of the disk, respectively, and $\phi_{\text{disk}} = 0.4\%$. It must be pointed out that such a hydrodynamic volume $[\phi_{\text{disk}}(4/3)(a/l)]$ is close to the excluded volume defined by Onsager²³ $[\phi_{\text{disk}}(\pi/2)(a/l)]$.

For such values of ϕ_{sphere} , multiple hydrodynamic interactions must be considered. In this context, the model developed by Quemada^{30,31} for dispersions relates suspension viscosity to effective volume fraction:

$$\eta_s = \eta_f \left[1 - \frac{\phi_{\text{eff}}}{\phi^*} \right]^{-2} \quad (9)$$

where η_s is the viscosity of the suspension, η_f is the viscosity of the suspending fluid, ϕ_{eff} represents an effective volume fraction corresponding to the hydrodynamic volume fraction of objects in the flow, and ϕ^* stands for the packing volume fraction. In the situation investigated here, the particles are obviously not oriented randomly for all shear rates, as revealed by the values of the (m_y , m_z) parameters (Table 1). The difficulty then consists of defining an appropriate hydrodynamic volume fraction that takes into account alignment phenomena while allowing an effective approach similar to that of Quemada. With increasing shear rate, the particles tend to gradually align along the velocity streamlines, which induces hydrodynamic drag reduction and consequently diminishes the viscosity of the suspension (Figure 10).

Under shear, the rotational degrees of freedom are restricted, and we assume that the geometrical volume encompassing the particles may be approximated by the ellipsoid described in

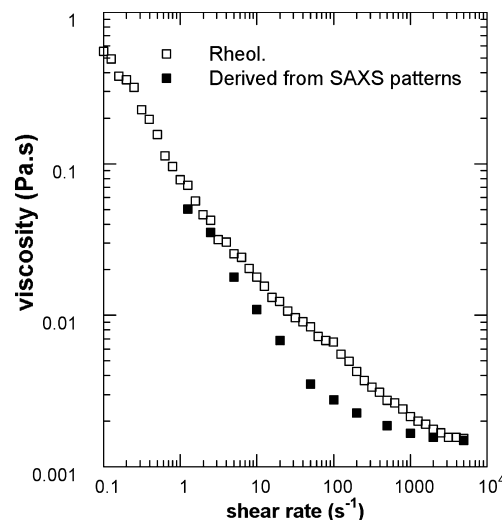
**Figure 10.** Comparison between experimental and calculated viscosities.

Figure 2. This reasoning is suggested by the similarities between the ellipsoid volume and the statistical volume including the particles, as discussed in section 2.3. Following this assumption, the effective volume fraction that may be considered in eq 9 is provided by

$$\phi_{\text{eff}} = \phi_{\text{sphere}} \frac{(4/3)\pi m_x m_y m_z}{(4/3)\pi m_x^3} = m_y m_z \phi_{\text{sphere}}$$

Use of eq 9 further requires the definition of a critical volume fraction ϕ^* . As shown in a previous study of nontronite suspensions,¹³ taking $\phi^* = 1$ provided a robust calculation of the interparticle distance between platelets and an acceptable estimate of the dependence of viscosity on volume fraction under infinite shear conditions.

Figure 10 compares the viscosity calculated from eq 9, following the arguments discussed above and using values of (m_y , m_z) displayed in Table 1, with that measured independently in a cone and plane geometry. The overall shear-thinning feature is well reproduced although the calculated curve is located at somewhat lower viscosity compared to experimental results. This difference stems from the fact that rheology and SAXS measurements were performed independently with two clay suspensions of similar concentrations but different batches, which could easily introduce 10% variation in ϕ . When rheology and SAXS experiments are carried out simultaneously in a rheometer cell, the comparison is optimized.³²

Despite this deviation, it should be stressed that, to the best of our knowledge, this study is the first to quantitatively relate rheological–SAXS patterns to a macroscopic rheological quantity such as viscosity.

6. Conclusion

The studies presented here demonstrate the interest of using small-angle X-ray scattering to describe the orientational field of platelets under shear flow. The anisotropies of the patterns recorded with a Couette shear cell in two different geometries (tangential and radial) show that particles present a biaxial orientation under shear. Pattern simulations based on a simple geometrical approach reveal that, on the length scale probed by SAXS ($< 0.3 \mu\text{m}$), the scattering anisotropy directly derives from the particle alignment in the shear-flow field. Moreover, this approach relates macroscopic properties like viscosity to

the structure of the dispersion. The suspension analyzed here exhibits marked shear-thinning properties, and the decrease of viscosity with the shear rate is related to the evolution of an effective volume in which particles are statistically confined. This type of analysis should be further extended to suspensions of particles with different size, aspect ratio, and shape (e.g., lath-shaped nontronite). Also, future developments should connect, at the particle length scale, the evolution of the suspension structure with other types of flow, like elongational flows. Such analyses will be addressed in a forthcoming article.

Acknowledgment. This work was financially supported by the French ANR agency (Agence Nationale de la Recherche, programme blanc ANISO). M. Imp  rator-Clerc is acknowledged for her participation in the experimental study. J.d.S. thanks the RTRA Triangle de la Physique (Orsay) for a postdoctoral fellowship. I.B. thanks Christian Bihannic for fruitful discussions.

References and Notes

- (1) Hunter, R. J. *Foundations of colloid science*; Oxford Science Publications: New York, 1995.
- (2) Hiemenz, P. C.; Rajagopalan, R. *Principles of colloid and surface chemistry*; Marcel Dekker, New York, 1997.
- (3) Callaghan, I. C.; Ottewill, R. *Faraday Discuss. Chem. Soc.* **1974**, 57, 110.
- (4) Vali, H.; Bachmann, L. J. *Colloid Interface Sci.* **1988**, 126, 278.
- (5) Lagaly, G. *Appl. Clay Sci.* **1989**, 4, 105.
- (6) G  ven, N. In *Clay-water interface and its rheological implications*; G  ven, N., Pollastro, R. M., Eds.; The Clay Minerals Society: Boulder, CO., 1992.
- (7) Ramsay, J. D. F.; Lindner, P. *J. Chem. Soc., Faraday Trans.* **1993**, 89, 4207.
- (8) Luckham, P. F.; Rossis, S. *Adv. Colloid Interface Sci.* **1999**, 82, 43.
- (9) Abend, S.; Lagaly, G. *Appl. Clay Sci.* **2000**, 16, 201.
- (10) Baravian, C.; Vantelon, D.; Thomas, F. *Langmuir* **2003**, 19, 8109.
- (11) Michot, L. J.; Bihannic, I.; Maddi, S.; Funari, S. S.; Baravian, C.; Levitz, P.; Davidson, P. *Proc. Natl. Acad. Sci. U.S.A.* **2006**, 103, 16101.
- (12) Michot, L. J.; Bihannic, I.; Maddi, S.; Baravian, C.; Levitz, P.; Davidson, P. *Langmuir* **2008**, 24, 3127.
- (13) Michot, L. J.; Baravian, C.; Bihannic, I.; Maddi, S.; Moyne, C.; Duval, J. F. L.; Levitz, P.; Davidson, P. *Langmuir* **2009**, 25, 127.
- (14) Michot, L. J.; Bihannic, I.; Maddi, S.; Duval, J. F. L.; Baravian, C.; Davidson, P.; Levitz, P.; *Clay Miner.* (in press).
- (15) Paineau, E.; Antonova, K.; Baravian, C.; Bihannic, I.; Davidson, P.; Dozov, I.; Imp  rator-Clerc, M.; Levitz, P.; Madsen, A.; Meneau, F.; Michot, L. J. *J. Phys. Chem. B* **2009**, 113, 15858.
- (16) Yamamoto, S.; Matsuo, T. *J. Chem. Phys.* **1997**, 107, 3300.
- (17) Hayter, J. B.; Penfold, J. *J. Chem. Phys.* **1984**, 88, 4589.
- (18) Hanley, H. J. M.; Straty, G. C.; Tsvetkov, F. *Langmuir* **1994**, 10, 3362.
- (19) Kalman, D. P.; Wagner, N. J. *Rheol. Acta* **2009**, 48, 897.
- (20) Maier, W.; Saupe, A. *Z. Naturforsch. A* **1958**, 13, 564.
- (21) Maier, W.; Saupe, A. *Z. Naturforsch. A* **1959**, 14, 882.
- (22) Maier, W.; Saupe, A. *Z. Naturforsch. A* **1960**, 15, 287.
- (23) Onsager, L. *Ann. N.Y. Acad. Sci.* **1949**, 51, 627.
- (24) Lemaire, B. J.; Panine, P.; Gabriel, J. C. P.; Davidson, P. *Europhys. Lett.* **2002**, 59, 55.
- (25) Fournet, G. *Bull. Soc. Fr. Mineral. Cristallogr.* **1951**, 74, 37.
- (26) Guinier, A.; Fournet, G. *Small-Angle Scattering of X-rays*; John Wiley and Sons: New York, 1951.
- (27) de Silva, J.; Peterman, D.; Kasmi, B.; Imp  rator-Clerc, M.; Davidson, P.; Pansu, B.; Meneau, F.; Perez, J.; Paineau, E.; Bihannic, I.; Michot, L. J.; Baravian, C.; *J. Phys.: Conf. Ser.* (in press).
- (28) Jeffery, G. B. *Proc. R. Soc. London, Ser. A* **1922**, 102, 161.
- (29) Risken, H.; *The Fokker-Planck equation. Methods of solutions and applications*; Springer: New York, 1999.
- (30) Quemada, D. *Rheol. Acta* **1977**, 16, 82.
- (31) Quemada, D.; Berli, C. *Adv. Colloid Interface Sci.* **2002**, 98, 51.
- (32) Phillipe, A. M.; Baravian, C.; Imp  rator-Clerc, M.; de Silva, J.; Paineau, E.; Bihannic, I.; Davidson, P.; Meneau, F.; Levitz, P.; Michot, L. J. *J. Phys.: Condens. Matter* (submitted for publication).

JP105714V